RSC Advances

PAPER

View Article Online
View Journal | View Issue

Cite this: *RSC Adv.*, 2026, **16**, 9806

An investigation on the electrochemical performance of Mn_3O_4-based aqueous symmetric supercapacitor devices

Chrisma Rose Babu, [ab] E. I. Anila, *[a] A. V. Avani,[a] Roshan Jose[c] and Xavier T. S [d]

Manganese (II, III) oxide (Mn_3O_4) is one of the promising materials in the realm of high-performance supercapacitors. The high theoretical specific capacitance, low cost, non-toxicity, environmental compatibility, and natural abundance made it significant in the research field. A low-temperature hydrothermal synthesis method was adopted to prepare Mn_3O_4 (hausmannite) nanoparticles with a tetragonal spinel structure. The as-prepared nanoparticles were assessed for the structural, elemental, electrical, optical and nitrogen adsorption–desorption studies through XRD, FTIR, Raman spectroscopy, XPS, DC conductivity, UV-vis absorption and BET analyses. Morphological studies were done using FESEM and TEM and a mixture of nanorods and nanocubes were observed. The electrochemical performances of the as-prepared Mn_3O_4 nanoparticles were investigated by cyclic voltammetry (CV), galvanostatic charge/discharge (GCD) method and electrochemical impedance spectroscopy (EIS) in a three-electrode system. The present work reports the fabrication of a prototype aqueous symmetric supercapacitor device for the first time. The electrochemical studies were performed in 0.5 M Na_2SO_4 electrolyte on the separator with a potential window of 0 V to 1 V. A specific capacitance of 68 Fg^{-1} at a current density of 1 Ag^{-1} was observed from the constant charge/discharge method. It exhibited a cyclic stability of 72% with a coulombic efficiency of 100% after 1000 cycles. This underscores the noteworthy role of manganese oxide nanoparticles as electrode materials in supercapacitors.

Received 11th November 2025
Accepted 21st January 2026

DOI: 10.1039/d5ra08702c

rsc.li/rsc-advances

1. Introduction

The increasing energy consumption has recently emerged as a severe focus to develop clean, sustainable, environmentally acceptable, and affordable energy resources. Considerable research has focused on this arena by promoting energy storage devices like batteries, supercapacitors and fuel cells. The demand for fast charge/discharge rates, cycle life, stability, power density and production costs consider supercapacitors as alternate energy storage devices for many applications in daily life. Supercapacitors are a power source for hybrid vehicles, electronic devices and grid systems. The performance of supercapacitors mainly depends on the properties of the electrode materials.[1–3] The electric double-layer capacitor and pseudocapacitor are two significant kinds of supercapacitors. The charge storage mechanism of these supercapacitors is classified into two: faradaic and non-faradaic charge storage. Electric double-layer capacitors (EDLC) comprise carbon compounds that undergo non-faradaic charge storage, whereas pseudocapacitors consist of either metal oxide-based or conducting polymer-based electrode materials that undergo a faradaic charge storage mechanism.[4,5]

Transition metal oxides play a vital role as electrode materials in pseudocapacitors because of their high energy and power density, which can store energy through quick faradaic redox reactions.[6,7] Various transition metal oxides like RuO_2,[8] Co_3O_4,[9] NiO,[10] MoO_3 (ref. 11) and manganese-based oxides are utilized for the fabrication of supercapacitor electrodes. Manganese oxides are considered promising electrode materials for their advantages: low cost, high power density, high specific capacitance, availability and environment-friendly nature. There are four different types of manganese oxides: MnO, MnO_2, Mn_2O_3 and Mn_3O_4 due to the presence of three kinds of oxidation states of manganese such as Mn^{2+}, Mn^{3+} and Mn^{4+}. Mn_3O_4 was the most stable oxide form among them.[12] Hausmannite nanostructures can be synthesized through the hydrothermal method,[13] co-precipitation,[14] sol–gel,[15] solvothermal,[16] microwave-assisted[17] and chemical reduction,[18] *etc.* Mn_3O_4 has a normal spinel structure at room temperature, in which Mn^{2+} ions are at the tetrahedral sites and Mn^{3+} ions are occupied at the octahedral sites.[19] It possesses a theoretical specific capacitance of 1400 Fg^{-1}, low electronic conductivity

[a]*Optoelectronic and Nanomaterials' Research Laboratory, Department of Physics and Electronics, CHRIST University, Bengaluru, Karnataka-560029, India. E-mail: anila.ei@christuniversity.in*

[b]*Cochin University of Science and Technology, Ernakulam, Kerala-682022, India*

[c]*Department of Physics, Marian College Kuttikkanam Autonomous, Idukki, Kerala-685531, India*

[d]*Government College for Women, Thiruvananthapuram, Kerala-695014, India*

and a wide potential window in the aqueous electrolyte medium.[20]

Wang *et al.*[21] synthesized Mn_3O_4 nanomaterials through a two-step hydrothermal method and produced a specific capacitance of 233.4 Fg^{-1} at a lower current density of 0.5 Ag^{-1}. A one-step hydrothermal method was followed by Prasad *et al.* for developing a Mn_3O_4 supercapacitor electrode with a specific capacitance of 147.5 Fg^{-1} at a current density of 0.5 Ag^{-1}.[22] Jiang *et al.*[13] found Mn_3O_4 nano-octahedrons through hydrothermal synthesis method to develop an electrode material that provides a specific capacitance of 244 Fg^{-1} at a scan rate of 5 mV s^{-1}. In all these works, electrochemical properties in a three-electrode configuration. Fabrication of symmetric supercapacitor device with Mn_3O_4 synthesized by hydrothermal method was done for the first time in this work.

The above-discussed works have inspired the present work to synthesize hausmannite Mn_3O_4 nanoparticles in a cost-effective way, without any surfactants or further calcination process. The structural, elemental, morphological, electrical, optical and surface properties were observed through X-ray diffraction studies (XRD), Fourier transform infrared spectroscopy (FTIR), Raman spectroscopy, transmission electron microscopy (TEM), X-ray photoelectron spectroscopy (XPS), field emission scanning microscopy (FESEM), DC conductivity, UV-visible absorption spectroscopy and Branauer Emmett Teller analyses. The fabrication of the Mn_3O_4 electrode presents a specific capacitance value of 163 Fg^{-1} at a current density of 4 Ag^{-1}, which was examined by the galvanostatic charge–discharge method. In this work, we report the fabrication of prototype aqueous symmetric supercapacitors for the first time with Mn_3O_4 electrodes prepared *via* simple hydrothermal method. The Mn_3O_4 symmetric supercapacitor device gained a specific capacitance of 68 Fg^{-1} at 1 Ag^{-1} with an energy density 9 W h kg^{-1}.

2. Experimental section

2.1. Chemicals

The chemical reagents used in the present work are of analytical grade and used without additional refinement. Sodium hydroxide and manganese chloride tetrahydrate were purchased from S. D. Fine Chem Ltd and Loba Chemie PVT. Ltd, respectively, India.

2.2. Preparation of Mn_3O_4 nanoparticles

For the synthesis of Mn_3O_4 nanoparticles, 1 M manganese chloride tetrahydrate ($MnCl_2 \cdot 4H_2O$) and 2 M sodium hydroxide (NaOH) taken in 25 mL distilled water separately were allowed for continuous stirring. NaOH was added dropwise to the manganese chloride precursor solution, forming a pale brown colloidal solution. The solution was then transferred to the 100 mL Teflon-lined autoclave. The solution underwent thermal treatment for 24 hours at 120 °C. After filtration and double-washing with distilled water, a dark brown product was obtained. It was dried at 60 °C to obtain pure Mn_3O_4 nanoparticles.

2.3. Material characterizations

X-ray diffraction studies were analyzed using the Rigaku Miniflex-XRD diffractometer with radiation of Cu Kα (1.5406 Å) working at 40 kV and 15 mA to determine the crystallinity of the as-prepared samples. By using Renishaw in Via Raman Microscope, the vibrational modes were identified through the Raman spectra. FTIR was observed using Shimadzu IR Spriti-L. Morphological analysis was done with Apero 2 FESEM (ThermoFisher Scientific). The elemental analysis was evaluated using a PHI-VERSAPROBE III X-ray photoelectron spectrometer. Altamira Instrument (model TB440A) was used for measuring specific surface area and pore size distribution through Brunaeur-Emmett-Teller (BET) and Barret-Joyner-Halenda (BJH) methods. DC conductivity studies were observed from Keithely 2450 SMU. The optical studies were done using a UV-1800 Shimadzu spectrophotometer. Electrochemical mechanisms were recorded using the CH instrument (CH660E).

2.4. Electrode fabrication and electrochemical tests

The supercapacitor electrode material was fabricated using nickel foam as the current collector. The nickel foam was cleaned by sonicating with acid, alkaline solutions and distilled water for few minutes. The working electrode was made up of Mn_3O_4 nanoparticles (80 wt% −0.0008 g), activated carbon (10 wt% −0.0001 g) as the conductive agent, and polytetrafluoroethylene (10% PTFE −0.0001 g) as the binder, which was sonicated in 2 ml ethanol and drop-casted on the substrate. The substrate used in the present work was a nickel foam of an area of 1 cm^2. The drop-casted electrodes were further dried at 60 °C for a few hours. The average mass loading was found to be 1 mg cm^{-2}. A three-electrode setup was assisted in analyzing the electrochemical performance of the active electrode material using cyclic voltammetry curves, galvanostatic charge–discharge curves and electrochemical impedance studies (1 M Hz to 1 Hz) at room temperature. The electrochemical mechanisms were performed in a CH (CHI660E) electrochemical workstation. The specific capacitance value (C_{sp}) can be observed from both cyclic voltammetry and charge–discharge analyses using the following equations:

$$C_{sp} = \frac{\text{Integrated Area under the curve}}{2mk\Delta V} \quad (1)$$

$$C_{sp} = \frac{I \times \Delta t}{m\Delta V} \quad (2)$$

where scan rate in volt per second (k), active mass loaded on the substrate in g (m), potential window in volt (ΔV), discharging time in seconds (Δt), and discharging current in Ampere (I). The energy density (E_D) and power density (P_D) can be calculated using the following equations,[23]

$$E_D = \frac{C_{sp}\Delta V^2}{2 \times 3.6} \quad (3)$$

$$P_D = \frac{E_D \times 3600}{\Delta t} \quad (4)$$

2.5. Preparation of Mn_3O_4//Mn_3O_4 symmetric supercapacitor device

The prototype aqueous symmetric supercapacitor device with the as-prepared Mn_3O_4 electrodes followed by sandwiching the two similar electrodes (1 cm^2 nickel foam with a thickness of 1.5 mm) separated by a separator. The Whatman filter paper (90 mm pore size) was taken as the separator for the device filled with 0.5 M Na_2SO_4 electrolyte solution.

3. Results and discussions

The crystal structure of the Mn_3O_4 nanoparticles were observed from the X-ray diffraction pattern as given in Fig. 1a. It corresponds to its normal spinel oxide with Mn^{2+} ions at the tetrahedral sites and Mn^{3+} at the octahedral sites (hausmannite). The predominant peaks were identified at 2θ values of 28.8°, 32.3°, 36.07° and 59.8°corresponding to (112), (103), (211) and (224) crystal planes. The other peaks with lower intensities correspond to the crystal planes of (101), (200), (004), (220), (105), (312), (303), (321), (224), (400), (206) and (413). No other impurity peaks were identified from the synthesized sample and the observed peaks are concordant with PDF card no: 9 001 963.[24]

The average crystallite size, D, can be measured from the Scherrer formula,

$$D = \frac{0.9\lambda}{\beta\cos\theta} \quad (5)$$

where the equation consists of full-width half-maximum–β, the wavelength–λ of Cu Kα 1.54 Å, shape factor–0.9 and Braggs angle–θ. The average crystallite, D was found to be 22 nm. The lattice parameters of the tetragonal phase structure can be identified from the given equation,[25]

$$\frac{1}{d^2} = \frac{h^2 + k^2}{a^2} + \frac{l^2}{c^2} \quad (6)$$

The calculated lattice constants, $a = b = 5.771$ Å and $c = 9.450$ Å which differ from those of bulk ($a = b = 5.769$ Å and $c = 9.460$ Å) due to size defect and presence of point defects. Structural refinements of Fig. 1a were performed using Profex software with a tetragonal structure and space group $I4_1/and$ (No. 141). The Rietveld-refined XRD pattern and the corresponding crystal structure are shown in Fig. S1 and S2. The reliability factors, atomic positions, and bond lengths between atoms are provided in Tables S1 and S2. The presence of the hausmannite phase is confirmed from the analysis.

The phase of the Mn_3O_4 nanoparticles can be confirmed by Raman spectroscopic analysis, a sensitive technique to identify the atomic vibrations and arrangements.[26] Fig. 1b shows the Raman spectra of the Mn_3O_4 nanoparticles synthesized through the hydrothermal method. The spectrum was analyzed, and some major peaks were found in the 300–700 cm^{-1} range. The single broad peak at 658 cm^{-1} agrees with the spinel structure of Mn_3O_4, which corresponds to the stretching mode (Mn–O) of Mn_3O_4, *i.e.*, A_{1g} mode. This mode explains the atomic vibrations of divalent manganese ions at the tetrahedral site which may be associated with Jahn–Teller distortion under certain conditions.[27] The other two major peaks were observed at 320 cm^{-1} and 373 cm^{-1} corresponding to the doubly degenerate T_{2g} (O–Mn–O) and E_g (Mn–O–Mn) symmetry modes respectively.[28] These observations confirm that no other secondary phase was formed which further agrees with the XRD results.

The chemical bonds present in the Mn_3O_4 nanoparticles were analyzed using Fourier transform infrared (FT-IR) spectroscopy as shown in Fig. 1c. The spectrum exhibits characteristic peaks at 611 cm^{-1} and 465 cm^{-1} which corresponds to the vibrations of Mn^{3+} ions at the octahedral sites. The absorption peak near 1095 cm^{-1} is attributed to Mn–OH vibrational modes. The peaks at 1625 cm^{-1} and 3392 cm^{-1} are associated with the presence of stretching and bending vibrations of water molecules adsorbed.[16,29,30]

The investigation structure and morphology of the Mn_3O_4 nanoparticles were analyzed from the transmission electron microscopy images. Fig. 2a and b showed the nanorods-like and distorted nanocube-like structures of Mn_3O_4 nanoparticles at different magnifications. The HR-TEM image revealed an interplanar spacing of 0.49 nm corresponding to the (101) crystal planes of Mn_3O_4 as given in Fig. 2c. The SAED (selected area electron diffraction) (Fig. 2d) pattern supports the fringe spacing observation and it exhibits the polycrystalline nature of Mn_3O_4. The surface morphology can be identified using field

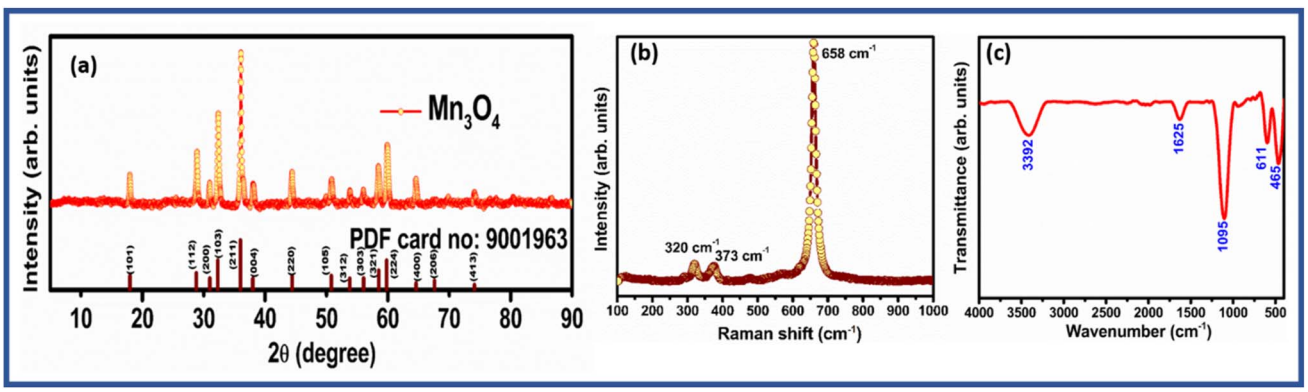

Fig. 1 (a). X-ray diffraction pattern, (b). Raman spectrum and (c). FTIR spectrum of Mn_3O_4 nanoparticles.

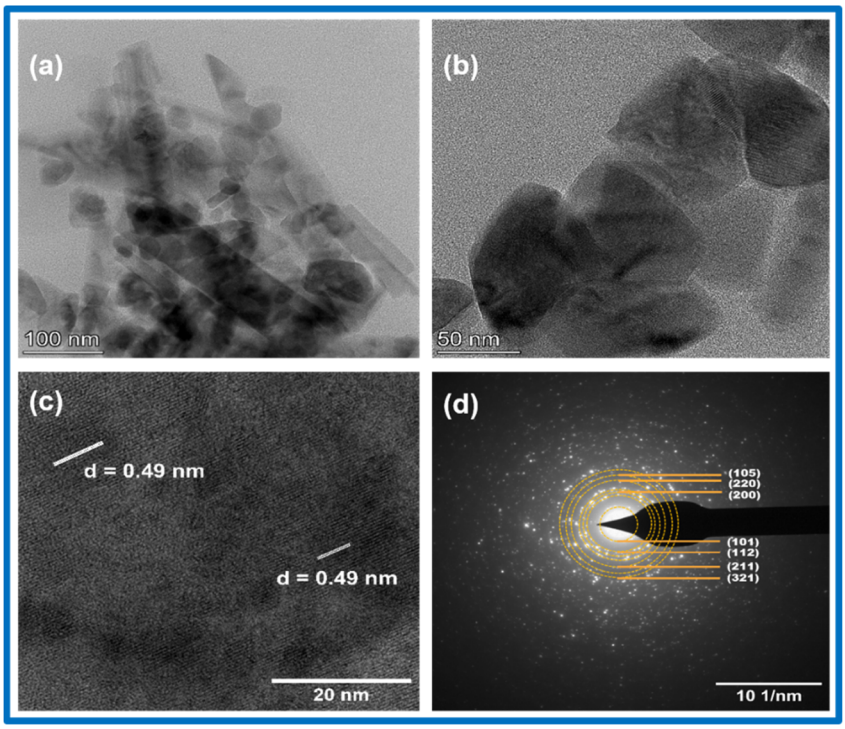

Fig. 2 (a and b). TEM images at different magnifications, (c). HR-TEM image and (d). SAED pattern of Mn_3O_4 nanoparticles.

emission scanning electron microscopy (FESEM). The FESEM image shows the mixture of distorted cube-like and rod-like structures at different magnifications are shown in Fig. 3. At high magnifications, the rod-like structures were covered with cube-like particles. An average particle size from 40–85 nm was observed for the cube-like structures. This kind of morphology promotes active sites for the application of supercapacitors.

The oxidation states and elemental composition of the Mn_3O_4 nanoparticles were analyzed from the X-ray photoelectron spectroscopy as shown in Fig. 4. The XPS survey was observed in the binding energy range between 0 to 1100 eV as given in Fig. 4a. No other impurities were significantly identified from the survey spectrum. The detailed spectrum of Mn 2p is shown in Fig. 4b. The major peaks of Mn $2p_{1/2}$ and Mn $2p_{3/2}$ were identified at binding energies of 652.5 eV and 641.0 eV, respectively. The spin–orbit splitting width between them was found to be 11.5 eV. The peak components of Mn $2p_{1/2}$ was deconvoluted into Mn^{2+} and Mn^{3+} at binding energies

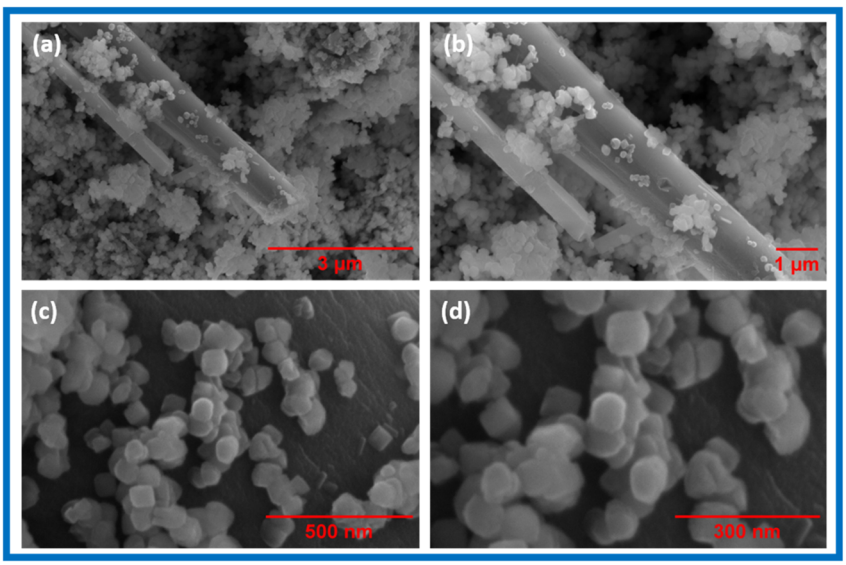

Fig. 3 FESEM images of Mn_3O_4 nanoparticles at different magnifications.

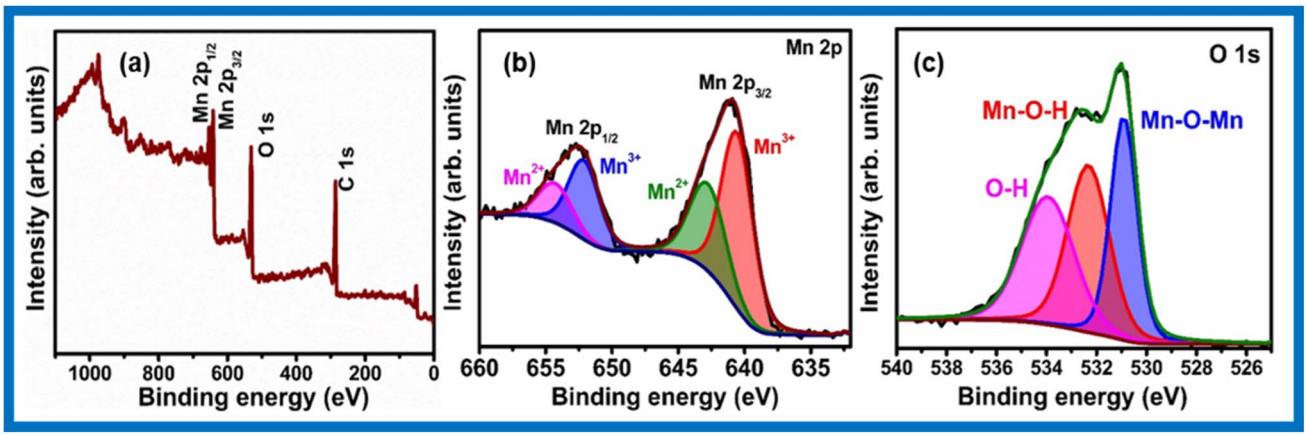

Fig. 4 (a). Survey spectrum, (b). Mn 2p spectrum and (c). O 1s spectrum of as-synthesized Mn_3O_4.

of 654.4 eV and 652.25 eV. Also, Mn $2p_{3/2}$ was deconvoluted into Mn^{2+} with a binding energy of 642.9 eV and Mn^{3+} with a binding energy of 640.75 eV.[31–34] The purity of the Mn_3O_4 compound can be confirmed by analyzing the O 1s spectrum given in Fig. 4c. The peaks at 530.2 eV, 532.3 eV and 533.9 eV correspond to the presence of Mn–O–Mn bond for oxide, Mn–O–H for hydroxide and O–H for residual water, respectively.[22,35]

The detailed curve-fitting of the Mn 2p XPS spectra confirms the presence of Mn^{2+} and Mn^{3+} oxidation states. The quantitative analysis determined the Mn^{2+} and Mn^{3+} fractions to be 36% and 64% based on Mn $2p_{3/2}$ peak area and 35% and 65% based on Mn $2p_{1/2}$ peak area, which resulted in the Mn^{2+}/Mn^{3+} ratio as ~0.54. The ratio confirms the mixed valence manganese oxide phase with a composition close to the stable hausmannite Mn_3O_4.[36]

The surface area and pore-size distributions of porous Mn_3O_4 nanoparticles were observed from the N_2 adsorption–desorption isotherms given in Fig. 5a. Type IV isotherm can be analyzed from the distinct hysteresis loop at high pressure region. The BET surface area obtained for the as-synthesized Mn_3O_4 is 15.25 $m^2\ g^{-1}$. The pore size distribution was observed through Barrett–Joyner–Halenda (BJH) method shown in Fig. 5b. The mesoporous nature of Mn_3O_4 nanoparticles was identified from the average pore diameter, 8.561 nm and it has an average pore volume of 0.033 $cm^3\ g^{-1}$. The BET surface area provided effective reaction sites for the accessibility of the electrolyte ions to the active electrode material for fast charging-discharging process.

The synthesized Mn_3O_4 nanoparticles were subjected to DC conductivity analysis using Keithley 2450 SMU conductivity meter. The conductivity studies were performed in a two-probe setup by pelletizing the obtained Mn_3O_4 powder. The pellet was found to be 12 mm in diameter and 36 mm in thickness. The electrical properties were analyzed based on the current *vs.* voltage characteristics. The conductivity obtained for the Mn_3O_4 nanoparticles was 9.38×10^{-6} S m^{-1} using the relation, conductivity is directly proportional to thickness of the pellet and inversely proportional to the product of area and electrical resistance.

The optical properties were observed from the UV-vis absorption analysis. The absorption spectrum was recorded in the range of 200–800 nm. The absorption peaks were found near 260 nm corresponds to the charge transfer transition at O^{2-} to Mn^{3+}. Fig. 6a demonstrates the change in the absorbance plot with respect to the wavelength of Mn_3O_4 nanoparticles. The optical energy band gap (E_g) of the material can be measured using the following equation:[37]

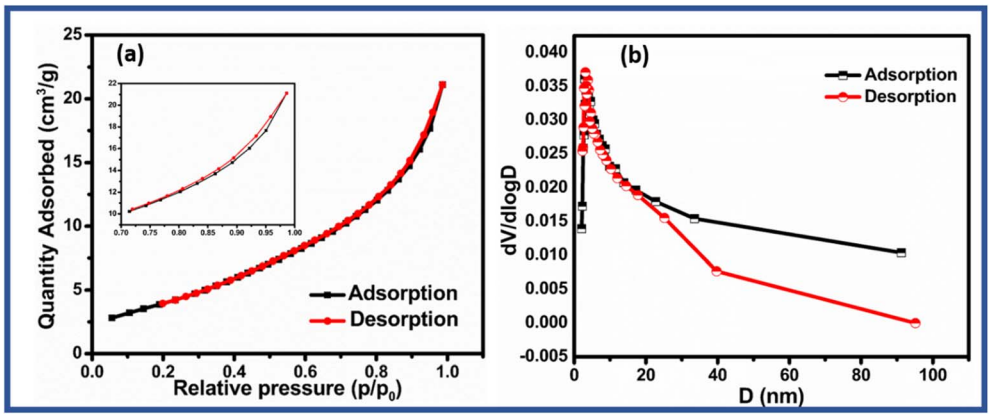

Fig. 5 (a). N_2 adsorption–desorption isotherm and (b). Pore size distribution of Mn_3O_4 nanoparticles.

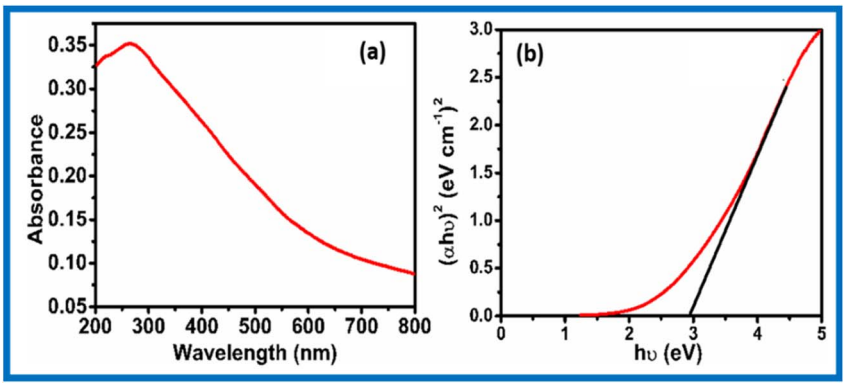

Fig. 6 (a). UV-vis absorption spectrum and (b). Tauc plot of Mn_3O_4 nanoparticles.

$$(\alpha h\vartheta)^{1/n} = A(h\vartheta - E_g) \quad (7)$$

The relation between phonon energy ($h\vartheta$), optical absorption coefficient (α), power factor of the transition mode (n) and proportionality constant or band tailing parameter (A). Here, Mn_3O_4 nanoparticles exhibit a direct band gap ($n = \frac{1}{2}$) energy of 2.99 eV as given Fig. 6b. The higher band gap was obtained due to the presence of size defects and it caused a blue shift from the bulk (2.3 eV).[38,39]

The electrochemical performance of the electrode material can be evaluated using cyclic voltammetry (CV) curves, galvanostatic charge–discharge (GCD), and electrochemical impedance spectroscopic (EIS) techniques. The capacitive behavior of the nickel foam-supported Mn_3O_4 nanoparticles was directly studied in aqueous 0.5 M Na_2SO_4 electrolyte solution at room temperature in a three-electrode setup. A potential window of −0.5 V to 0.2 V was investigated for the CV and GCD analysis at different scan rates and current densities, respectively. The three-electrode setup consists of a working electrode (Mn_3O_4 drop-casted on Ni foam), a reference electrode (Ag/AgCl) and a counter electrode (Platinum).

The cyclic voltammograms of Mn_3O_4 nanoparticles were observed for different scan rates ranging from 1 mV s^{-1} to 1000 mV s^{-1} as shown in Fig. 7a. All the CV curves are identified to be quasi-rectangular shape which exhibits the capacitive kind behaviour in its nature. This property would enhance its electrochemically reversible nature along with faradaic redox reactions. The CV curves also exhibit an ideal electrochemical capacitive behaviour. The mechanism of charge storage during the charging and discharging can be expressed as follows:

$$Mn_3O_4 \xrightarrow{\text{Charging}} Na_\delta MnO_x \cdot nH_2O \text{ (birnessite)} \quad (8)$$

$$Na_\delta MnO_x \cdot nH_2O + yH^+ + zNa^+ + (y+z)e^- \leftrightarrow H_yNa_{\delta+z}MnO_x \cdot nH_2O \quad (9)$$

The Na^{2+} ions in the electrolyte solution move towards the fabricated Mn_3O_4 electrode and occupy the available sites on the surface and on the inner portion also at lower scan rates. On the other hand, it will be difficult for the ions to occupy the available sites of the Mn_3O_4 electrode at higher scan rates.[40] This is due to the partial movement of ions in the electrolyte solution. The formation of spinel Mn_3O_4 to layered birnessite can be observed from the first reaction represented by eqn (8), which is an irreversible and complex process. The second reaction eqn (9) confirms the reversibility of the product obtained.[3] These two mechanisms occurred due to the adsorption of solvated cations which leads to the lowering of binding energy. The oxidation of Mn^{2+} to Mn^{3+} occurs during the cathodic sweep. This will result in a change in the oxidation number of manganese. Also, the reduction of Mn^{3+} to Mn^{2+} occurs during the anodic sweep; this, in turn, reduces the average oxidation number of manganese.[41] Fig. 7b shows the variation of specific capacitance value with the scan rates. A decrease in the specific capacitance value can be observed on increasing the scan rate. This nature of the electrode material confirms the capacitive behaviour of the fabricated Mn_3O_4 electrode. From the CV curves, the specific capacitance value was found to be 436 Fg^{-1} at a scan rate of 1 mV s^{-1}. The nature of charge storage mechanism of the electrode can be analyzed using Dunn's method. From the Power law,

$$i = av^b \quad (10)$$

$$\log i = \log a + b \log v \quad (11)$$

A b-value of 0.5 indicates the faradaic capacitive process and 1.0 corresponds to non-faradaic process. The b-value obtained for Mn_3O_4 electrode was 0.83, which indicates the pseudocapacitive behaviour (both faradaic and non-faradaic mechanisms coexists) of the Mn_3O_4 electrode (Fig. 7c). The contribution studies of capacitive or diffusion-controlled nature of electrodes were analyzed from the Dunn's method using the following equations,

$$i = k_1 v + k_2 v^{1/2} \quad (12)$$

$$i/v^{1/2} = k_1 v^{1/2} + k_2 \quad (13)$$

The surface or capacitive-controlled contribution is represented by $k_1 v$ and $k_2 v^{1/2}$ gives the diffusion-controlled

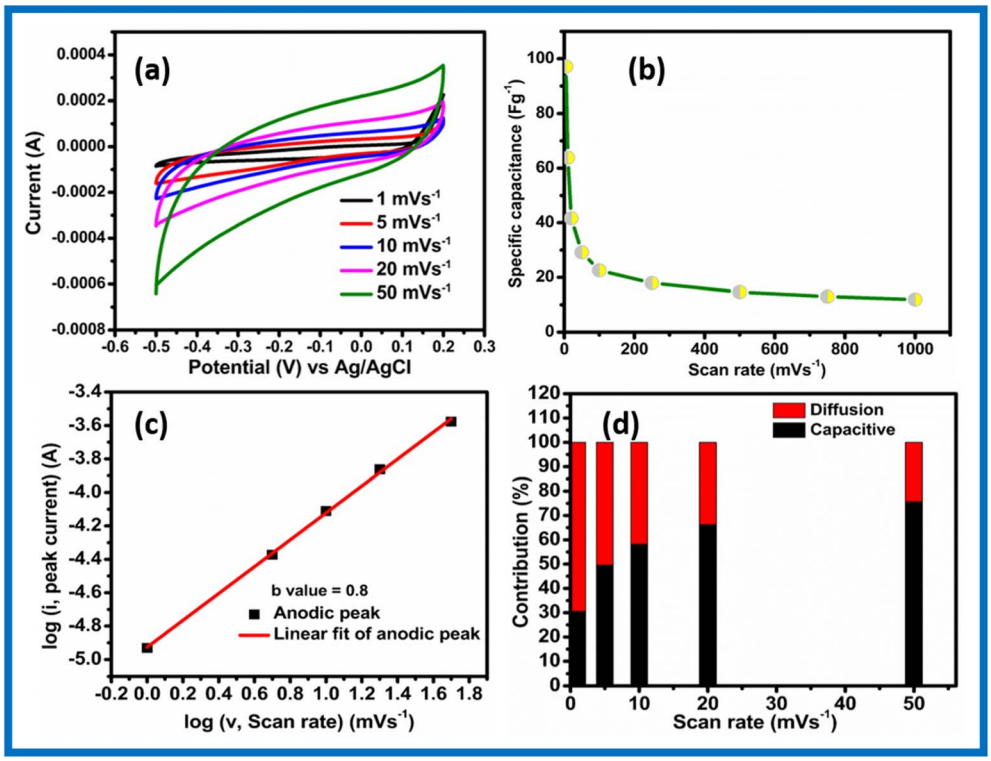

Fig. 7 (a and b). Cyclic voltammogram and (c). relationship between specific capacitance and scan rate (mV s^{-1}).

contribution.[42] Fig. 7d shows the surface-controlled and diffusion-controlled behaviour of Mn_3O_4 electrode from the cyclic voltammetric analyses.

The charge–discharge mechanism of the Mn_3O_4 electrode was observed from the galvanostatic charge–discharge method, as shown in Fig. 8a. The charge–discharge curves of Mn_3O_4 were observed at different current densities in the potential range between −0.5 V to 0.2 V. Fig. 8b shows the variation of the specific capacitance value according to the current densities. A significant reduction in the capacitance with respect to the increase in the current density is due to the potential drop observed in the discharging curves because of the resistance of the electrode. It can also be due to the insufficient redox reactions at the electrode/electrolyte interface at higher current densities.[43] The non-linear curves identified from the charge–discharge curves indicate the pseudocapacitive nature of the Mn_3O_4 electrode.[41] The specific capacitance value obtained at a current density of 4 Ag^{-1} is found to be 163 Fg^{-1}. The redox effect of the Mn_3O_4 electrode can be analyzed from the GCD curves.

Further investigation of the electrochemical properties was done with electrochemical impedance spectroscopy (EIS) and the equivalent fitted diagram, as given in Fig. 8c. The Nyquist plots describe the ohmic property (Z′) and capacitive property (–Z″). It consists of three regions: high-frequency, middle-frequency, and low-frequency regions. The equivalent circuit

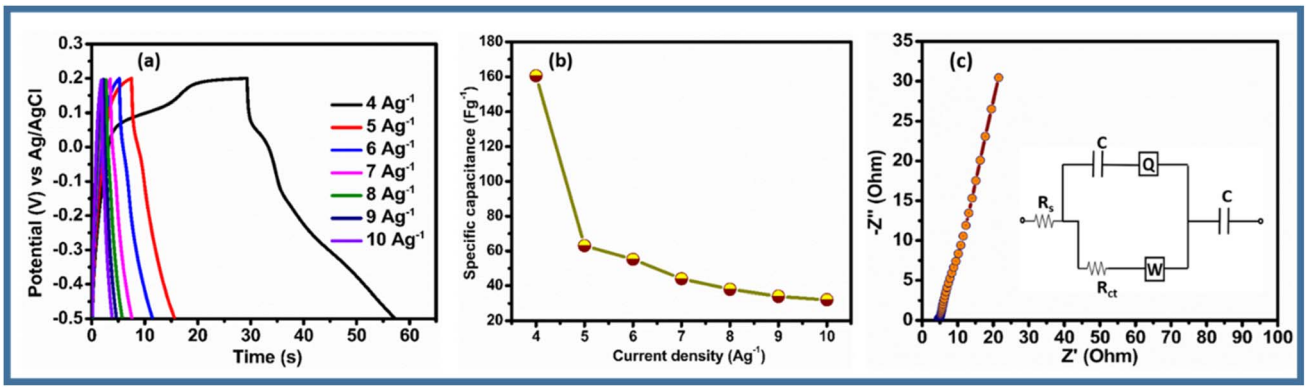

Fig. 8 (a). Chronopotentiometric curves, (b). specific capacitance as a function of the current density and (c). Nyquist plot (inset: fitted equivalent circuit diagram of the analyzed EIS data) of Mn_3O_4 electrode.

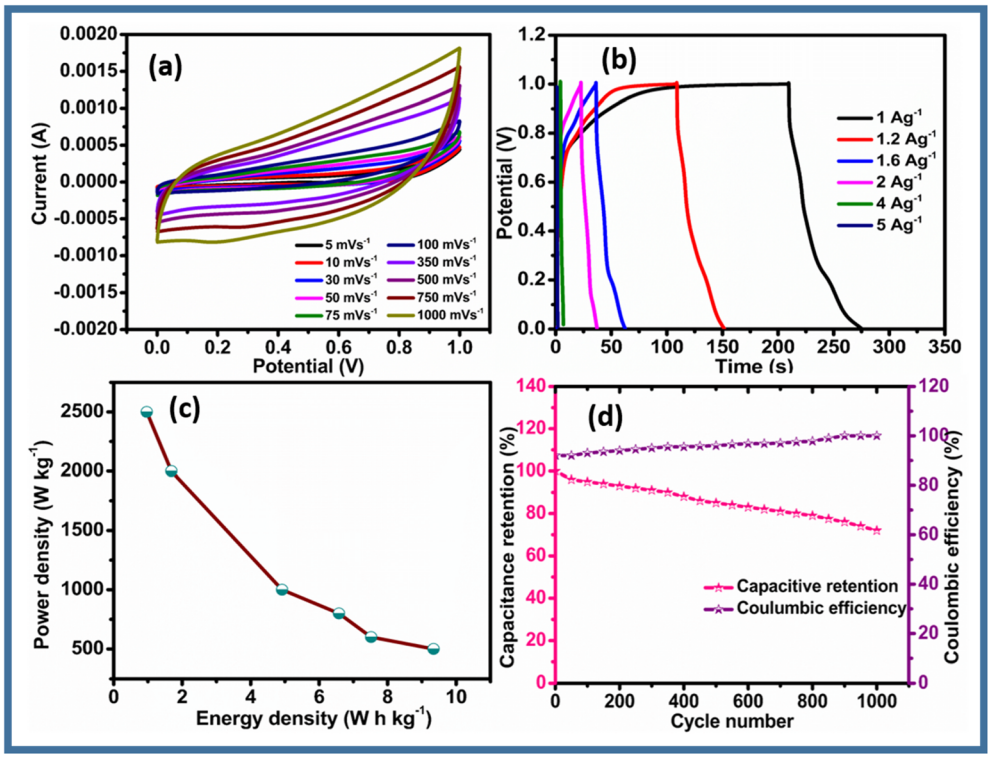

Fig. 9 Prototype aqueous symmetric supercapacitor device studies with (a). CV, (b). GCD, (c). Ragone plot and (d). Cyclic stability and coulombic efficiency over 1000 cycles.

diagram consists of the solution resistance (R_s), charge-transfer resistance (R_{ct}), the Warburg diffusion element (W) and the constant phase element (Q). The equivalent series resistance (R_s) is given by the x-intercept of the curve, 4.61 Ω. The interface or charge transfer resistance of the electrode material can be identified from the diameter of the semicircle region of the Nyquist plot which was found to be 0.25 Ω. This semicircle formation occurred due to the faradaic reactions at the electrode/electrolyte interface. The lower the diameter of the semicircle, the lesser the interface resistance and it enhances the utilization of the active electrode surface.[21] The linear region obtained in the low-frequency region corresponds to the typical capacitive behavior of the Mn_3O_4 electrode.[44] Fig. S3 (a–c) shows the cyclic voltammogram, charge–discharge curves and Nyquist

Table 1 Comparison of the electrochemical performance of Mn_3O_4 based symmetric supercapacitor with other metal oxide-based symmetric supercapacitors

Material in device form	Synthesis	Substrate	Current density (Ag^{-1} or mA cm^{-2})/ Scan rate (mV s^{-1})	C_{sp} (Fg^{-1})	E_D (W h kg^{-1})	Ref.
NiO//NiO	Atomic layer deposition	ITO@PET	10 μA cm^{-2}	0.612 mF cm^{-2}	0.0544 μ Wh cm^{-2}	45
MnO_2//MnO_2	Hydrothermal	Nickel foam	0.5 Ag^{-1}	181	3.4	46
Fe_2O_3@ACC// Fe_2O_3@ACC	Hydrothermal	Carbon cloth	1 mA cm^{-2}	1565 mF cm^{-2}	0.0092	47
MoO_3//MoO_3	Electrodeposition	Carbon cloth	1 Ag^{-1}	141	78	48
V_2O_5@AC//V_2O_5@AC	Hydrothermal	Carbon fabric	2.77 mg cm^{-2}	135	48.32	49
Co_3O_4//Co_3O_4	Hydrothermal	Nickel foam	5 Ag^{-1}	870.6	77.3	9
ZnO//ZnO	Sol–gel	Cellulose nanofibers	1 Ag^{-1}	220	30.2	36
Mn_3O_4//Mn_3O_4	Chemical precipitation with cocosin	Nickel foil	1 Ag^{-1}	203.8	91.7	50
Mn_3O_4//Mn_3O_4	Successive ionic layer adsorption and reaction	Stainless steel	2 mA cm^{-2}	72	1.3	51
Mn_3O_4//Mn_3O_4	Microwave-assisted chemical route	Stainless steel coin	1.27 mA cm^{-2}	665.08	0.0789	52
Mn_3O_4//Mn_3O_4	Hydrothermal	Nickel foam	1 Ag^{-1}	68	9	Present work

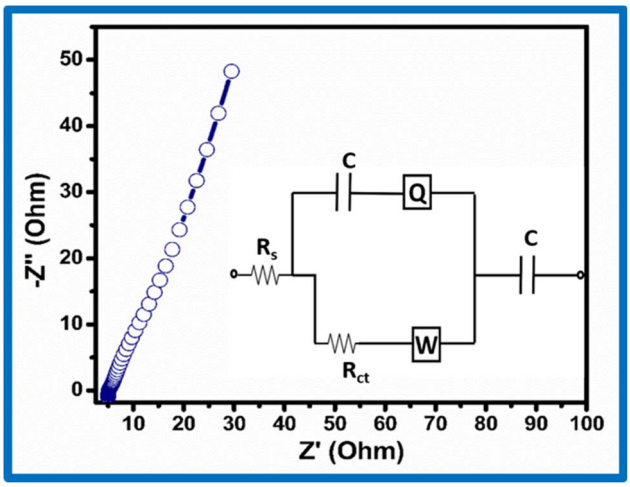

Fig. 10 Nyquist plot of Mn_3O_4//Mn_3O_4 symmetric supercapacitor device.

plot of bare Ni foam under the same electrochemical conditions where the active material was studied. The electrochemical behaviour of the Ni foam is very poor and it could be studied to analyze the enhancement of the capacitive property of the active material (Mn_3O_4) after drop-casting. The specific capacitance of the Ni foam with an imaginary mass loading of 1 mg is 18.4 Fg^{-1} at a current density of 4 Ag^{-1}, which is very low compared to the specific capacitance obtained for Mn_3O_4. The redox peaks were negligible from the CV and GCD curves, revealing the absence of Ni oxidation during the electrochemical processes. The Nyquist plot was also observed in the same electrochemical conditions of Mn_3O_4 and revealed the difference in the electrochemical behaviour of the active material.

3.1 Prototype aqueous symmetric device studies

The observations from the preliminary studies exhibited a better electrochemical performance of Mn_3O_4 electrode. A prototype symmetric supercapacitor device was fabricated with an average mass loading of 1 mg per electrode. The device was analyzed in 0.5 M Na_2SO_4 electrolyte solution in a potential window of 0–1 V. The CV curves obtained for the device was analyzed within a scan rate of 5 mV s^{-1} to 1000 mV s^{-1}. The redox peaks in CV curves were not clearly evident and the curves are not changing drastically with the increase of scan rates. The reversibility of the faradaic reactions can be examined from Fig. 9a. The charge storage mechanism at lower scan rate allows Na^+ ions in the electrolyte get inserted into the available pores on the surface of the electrode and also to the inner sides of Mn_3O_4. The effective interaction of ions and electrode would be reduced at higher scan rate which decreases the specific capacitance values.

Capacitive performance can be acquired from the galvanostatic charge–discharge curves (Fig. 9b). As the current density increases, the specific capacitance value decreases (Fig. 9c). The distortion in the linear nature of charge–discharge curves can be due to the high internal resistance between the electrode/electrolyte interface of the device. The discharging process exhibits a higher specific capacitance at lower current densities. The specific capacitance obtained at 1 Ag^{-1} is 68 Fg^{-1} with an energy density of 9.34 W h kg^{-1} and a power density of 500 W kg^{-1}. The device showed a cyclic stability of 72% after 1 k cycles of charging and discharging (Fig. 9d). The coulombic efficiency of the Mn_3O_4//Mn_3O_4 device initiates at 92% and gradually it increases and remained consistent at 100% after 850th cycle up to 1000th cycle. Table 1 shows a comparison of symmetric prototype devices with respect to other reports of Mn_3O_4 and other materials. The energy density of our material is better compared to other reports of Mn_3O_4 symmetric devices except the work in which Mn_3O_4 prepared with cocosin through chemical precipitation method.

The electrochemical impedance spectroscopy (EIS) studies observed the solution resistance and charge transfer resistance in a frequency range of 1 Hz to 1 M Hz (Fig. 10). The solution resistance (R_s) is found to be 5 Ω and a charge transfer resistance (R_{ct}) is 0.35 Ω were identified from the fitted circuit diagram. The linear variation at the low-frequency region in the Nyquist plot determines the Warburg resistance, which is observed due to the ion diffusion. It is one of the significant properties of supercapacitor applications.[53]

4. Conclusion

Hausmannite Mn_3O_4 nanoparticles were synthesized at a low temperature by hydrothermal method. The obtained Mn_3O_4 nanoparticles showed a tetragonal spinel structure confirmed by the XRD and Raman spectrum analyses. Mn^{2+} and Mn^{3+} oxidation states were observed from the Mn 2p spectrum through XPS. The morphological analysis found a mixture of nanocubes and nanorods in the as-synthesized Mn_3O_4 nanoparticles. The optical band gap was observed near 2.99 eV. The investigation of the electrochemical performance was observed from the cyclic voltammetry curves, galvanostatic charging/discharging curves and impedance plots. A prototype aqueous symmetric supercapacitor was fabricated to study the device-level performance in a working potential window of 1 V. The device exhibited a specific capacitance of 63 Fg^{-1} at 1 Ag^{-1} with an energy density of 9 W h kg^{-1} and power density of 500 W kg^{-1}.

Author contributions

Chrisma Rose Babu: conceptualization, methodology, validation, formal analysis, investigation, writing – original draft, writing – review and editing. E. I. Anila: methodology, writing – original draft, writing – review and editing, supervision, validation. A. V. Avani: methodology, writing – review and editing. Roshan Jose: formal analysis and writing. Xavier T. S: formal analysis and data curation.

Conflicts of interest

The authors declare that they have no known competing financial interests or personal relationships that could have appeared to influence the work reported in this paper.

Data availability

The data supporting the findings of this study are available within the article and its supplementary information (SI). Supplementary information is available. See DOI: https://doi.org/10.1039/d5ra08702c.

Acknowledgements

This research work was supported by Centre for Advanced Research and Development (CARD), CHRIST (Deemed to be University), Bangalore, Karnataka.

References

1 D. P. Dubal, D. S. Dhawale, R. R. Salunkhe, S. M. Pawar and C. D. Lokhande, *Appl. Surf. Sci.*, 2010, **256**, 4411–4416.
2 P. Suktha, N. Phattharasupakun, P. Dittanet and M. Sawangphruk, *RSC Adv.*, 2017, **7**, 9958–9963.
3 B. Gnana Sundara Raj, A. M. Asiri, J. J. Wu and S. Anandan, *J. Alloys Compd.*, 2015, **636**, 234–240.
4 R. B. Chrisma, R. I. Jafri and E. I. Anila, *J. Mater. Sci.*, 2023, **58**, 6124–6150.
5 T. Kansaard, T. Singha, S. Wannapop, A. Boonkitkoson, Y. Chuminjak, J. Sodtipinta and A. Somdee, *J. Alloys Compd.*, 2025, **1010**, 178185.
6 Z. S. Doroudkhani, J. Mazloom and M. M. Ghaziani, *Sci. Rep.*, 2025, **15**, 1–17.
7 B. J. Rani, M. Ravina, G. Ravi, S. Ravichandran, V. Ganesh and R. Yuvakkumar, *Surf. Interfaces*, 2018, **11**, 28–36.
8 R. Ge and L. Chen, *Adv. Compos. Hybrid Mater.*, 2022, **5**, 696–703.
9 C. R. Babu, A. V Avani, T. S. Xavier, M. Tomy, S. Shaji and E. I. Anila, *J. Energy Storage*, 2024, **80**, 110382.
10 X. Huang, Z. Yin, S. Wu, X. Qi, Q. He, Q. Zhang, Q. Yan, F. Boey and H. Zhang, *Small*, 2011, **7**, 1876–1902.
11 L. Wang, L. Gao, J. Wang and Y. Shen, *J. Mater. Sci.*, 2019, **54**, 13685–13693.
12 E. Yu, Y. M. Kang and W. D. Yang, *Electrochim. Acta*, 2025, **513**, 145520.
13 H. Jiang, T. Zhao, C. Yan, J. Ma and C. Li, *Nanoscale*, 2010, **2**, 2195–2198.
14 S. Jamil, S. R. Khan, B. Sultana, M. Hashmi, M. Haroon and M. R. S. A. Janjua, *J. Cluster Sci.*, 2018, **29**, 1099–1106.
15 V. C. Bose, K. Maniammal, G. Madhu, C. L. Veenas, A. S. A. Raj and V. Biju, *IOP Conf. Ser. Mater. Sci. Eng.*, 2015, **73**, 012084.
16 K. A. M. Ahmed and K. Huang, *Arab. J. Chem.*, 2019, **12**, 429–439.
17 M. Shahid, T. R. Katugampalage, M. Khalid, W. Ahmed, C. Kaewsaneha, P. Sreearunothai and P. Opaprakasit, *Sci. Rep.*, 2022, **12**, 1–16.
18 V. C. Bose and V. Biju, *Phys. E*, 2015, **66**, 24–32.
19 B. G. S. Raj, R. N. R. Ramprasad, A. M. Asiri, J. J. Wu and S. Anandan, *Electrochim. Acta*, 2015, **156**, 127–137.
20 D. P. Shaik, R. Pitcheri, Y. Qiu and O. M. Hussain, *Ceram. Int.*, 2019, **45**, 2226–2233.
21 Z. Wang, J. Fang, Y. Hao, C. Chen and D. Zhang, *Mater. Sci. Semicond. Process.*, 2021, **130**, 105823.
22 K. Prasad, T. V. M. Sreekanth, K. Yoo and J. Kim, *Vacuum*, 2024, **221**, 112930.
23 C. R. Babu, E. I. Anila and A. V Avani, *Fuel*, 2026, **406**, 137225.
24 H. Dhaouadi, A. Madani and F. Touati, *Mater. Lett.*, 2010, **64**, 2395–2398.
25 A. Rizky, A. Fadhillah, Irzaman and Irmansyah, *J. Phys., Conf. Ser.*, 2021, **2019**, 012070.
26 D. P. M. D. Shaik, P. Rosaiah and O. M. Hussain, *Mater. Today Proc.*, 2016, **3**, 64–73.
27 T. Larbi, K. Doll and T. Manoubi, *J. Alloys Compd.*, 2016, **688**, 692–698.
28 Z. Y. Tian, P. Mountapmbeme Kouotou, N. Bahlawane and P. H. Tchoua Ngamou, *J. Phys. Chem. C*, 2013, **117**, 6218–6224.
29 Y. Luo, W. Tan, S. L. Suib, G. Qiu and F. Liu, *Chem. Geol.*, 2018, **487**, 54–62.
30 M. Jarvin, S. A. Kumar, G. Vinodhkumar, E. Manikandan and S. S. R. Inbanathan, *Mater. Lett.*, 2021, **305**, 130750.
31 Z. Ren, W. Wu, L. Yu and Y. Yu, *Environ. Sci. Pollut. Res.*, 2019, **26**, 36776–36785.
32 B. Gnana Sundara Raj, A. M. Asiri, J. J. Wu and S. Anandan, *J. Alloys Compd.*, 2015, **636**, 234–240.
33 A. Moses Ezhil Raj, S. G. Victoria, V. B. Jothy, C. Ravidhas, J. Wollschläger, M. Suendorf, M. Neumann, M. Jayachandran and C. Sanjeeviraja, *Appl. Surf. Sci.*, 2010, **256**, 2920–2926.
34 V. C. Bose and V. Biju, *Bull. Mater. Sci.*, 2015, **38**, 865–873.
35 R. Aswathy, M. Ulaganathan and P. Ragupathy, *J. Alloys Compd.*, 2018, **767**, 141–150.
36 I. Rabani, J. Yoo, C. Bathula, S. Hussain and Y. S. Seo, *J. Mater. Chem. A*, 2021, **9**, 11580–11594.
37 B. Jos, C. R. Babu, S. Shaji and E. I. Anila, *J. Mater. Sci. Mater. Electron.*, 2024, **35**, 233.
38 N. M. Hosny and A. Dahshan, *Mater. Chem. Phys.*, 2012, **137**, 637–643.
39 R. Vignesh, R. Sivakumar and C. Sanjeeviraja, *Opt. Mater.*, 2021, **111**, 110580.
40 F. Zhang, X. G. Zhang and L. Hao, *Mater. Chem. Phys.*, 2011, **126**, 853–858.
41 S. G. Sayyed, H. M. Pathan, A. V. Shaikh, S. F. Shaikh and A. M. Al-Enizi, *J. Energy Storage*, 2021, **33**, 102076.
42 Y. Shao, M. F. El-Kady, J. Sun, Y. Li, Q. Zhang, M. Zhu, H. Wang, B. Dunn and R. B. Kaner, *Chem. Rev.*, 2018, **118**, 9233–9280.
43 D. Li, F. Meng, X. Yan, L. Yang, H. Heng and Y. Zhu, *Nanoscale Res. Lett.*, 2013, **8**, 1–8.
44 A. A. Yadav, S. N. Jadhav, D. M. Chougule, P. D. Patil, U. J. Chavan and Y. D. Kolekar, *Electrochim. Acta*, 2016, **206**, 134–142.
45 T. Kavinkumar, A. T. Sivagurunathan and D.-H. Kim, *Appl. Surf. Sci.*, 2023, **616**, 156453.
46 R. S. Kalubarme, H. S. Jadhav and C. J. Park, *Electrochim. Acta*, 2013, **87**, 457–465.
47 J. Li, Y. Wang, W. Xu, Y. Wang, B. Zhang, S. Luo, X. Zhou, C. Zhang, X. Gu and C. Hu, *Nano Energy*, 2019, **57**, 379–387.

48 N. Zhao, H. Fan, M. Zhang, J. Ma, Z. Du, B. Yan, H. Li and X. Jiang, *Chem. Eng. J.*, 2020, **390**, 124477.
49 K. Panigrahi, P. Howli and K. K. Chattopadhyay, *Electrochim. Acta*, 2020, **337**, 135701.
50 J. Yesuraj, S. Vajravijayan, R. Yang, N. Nandhagopal, K. Gunasekaran, N. C. S. Selvam, P. J. Yoo and K. Kim, *Langmuir*, 2022, **38**, 2928–2941.
51 D. P. Dubal, A. D. Jagadale and C. D. Lokhande, *Electrochim. Acta*, 2012, **80**, 160–170.
52 V. C. Bose and V. Biju, *Bull. Mater. Sci.*, 2015, **38**, 865–873.
53 C. R. Babu, A. V. Avani and E. I. Anila, *Int. J. Hydrogen Energy*, 2025, **109**, 242–253.